GRASP model description & validation report

Version 1.0
December 5, 2019

Evert Wiegant[1] and Remco Verzijlbergh[1]

[1]Whiffle Weather Finecasting Ltd, Molengraaffsingel 12, 2629 JD Delft, the Netherlands

ABSTRACT

Multi-year Large Eddy Simulations were performed around 3 offshore wind farm sites. The model setup is described, together with a short overview of its results. The simulation data is found to agree well with observations at most sites regarding scores such as correlation and bias.

Introduction

The Dutch Offshore Wind Atlas (DOWA) project addressess the reduction of uncertainties in wind and wind energy modelling on the Dutch North Sea. The central task of Whiffle in the DOWA project is to implement a wind turbine parameterization in its LES model and to perform LES runs for several offshore wind energy zones. This document describes the employed model and its validation against the Dutch offshore wind farm zones Borssele, Hollandse Kust Zuid and Hollandse Kust Noord.

Description of method

Whiffle uses its GPU-Resident Atmospheric Simulation Platform (GRASP) to perform calculations of the wake effects of the HKN wind farm. GRASP is a Large Eddy Simulation model that performs its core routines on Graphics Processing Units (GPUs). The origin of GRASP lies in an LES code that is commonly referred to as DALES: Dutch Atmospheric Large Eddy Simulation, see [Heus et al., 2010]. DALES has been and is still widely used in the boundary layer meteorology community. To overcome the barrier of the large computational costs that have long prohibited the use of LES in operational weather forecasting, the DALES model was translated to a code that runs most of its computational routines on GPUs [Schalkwijk et al., 2012].

Sites

Three areas at or around planned wind farm zones were simulated using GRASP. The sites are the Borssele wind farm zone (BWFZ), the Hollandse Kust Noord (HKN) WFZ, and the Hollandse Kust Zuid (HKZ) WFZ. Wind farms at these three sites have recently been tendered (BWFZ and HKZ) or will be tendered soon (HKNWFZ). As a part of the tendering procedure, RVO has organised floating LiDAR measurement campaigns that provide useful data to compare the model results with.

Time periods

Different time periods were selected for each site that seemed most relevant regarding present measurement campaigns and operation of present turbines. Unfortunately, for the Borssele and HKN sites, a number of days are missing as a result of missing or incorrect large-scale weather input data. Below we describe the simulated periods and missing days for all sites.

Borssele

The simulation at Borssele is done for the years 2015, 2016 and 2017 (3 years total). Missing days are noted in table 1.

Month	Dates
Aug. 2016	28
May 2017	12

Table 1. Missing days for the simulation at the Borssele site.

Month	Dates
Jan. 2009	1
Feb. 2010	28
Mar. 2010	2, 3, 4, 5, 8, 9, 10, 11, 12, 14, 15, 17, 18, 19, 20, 24, 26
Apr. 2010	1, 3, 5, 7, 22, 24

Table 2. Missing days for the simulation at the HNK site.

Hollandse Kust Noord

The simulations at HKNWFZ are performed for the years 2009, 2010, 2017 (3 years total). Missing days are noted in table 2.

Hollandse Kust Zuid

The simulations at HKZ are done for the years 2016, 2017, 2018 up to and including July 30 (about 2.5 years total). No days are missing for this simulation.

Domain & resolution

All simulations were performed using equivalent resolutions and domain sizes (measured in meters). The domains extend 32768m in horizontal (x and y) directions and ∼5000/1500m in the vertical (z) direction for the precursor/cursor (see section 2.5 for the description of the precursor concept). The vertical directions are each divided in 512 grid cells, resulting in grid cell sizes of 64m in either direction. The vertical direction is divided in 96/48 (precursor/cursor) cells. The height of grid cells increases towards higher altitudes, with the bottom level chosen to be 20m high. Grid cells at higher levels are ∼1.79% larger than one cell below. At the top of the domain, the grid cells have grown to 108/46m in the precursor/cursor.

Projection

To translate coordinates of the native (cartesian) GRASP grid to WGS 84 coordinates, the gnomonic projection is used. The centre of the domain serves the centre of the projection, which is matched to a chosen coordinate in the WGS 84 system. The projection slightly reduces distances as they are measured in WGS 84 with respect to how they were measured in GRASP coordinates. To counteract this reduction, the cartesian grid is slightly enlarged (by means of typical map scaling) before/after translation when translating to/from WGS 84 coordinates.

Translation between coordinates of native (cartesian) GRASP and WGS84 coordinates is done using the Gnomonic projection. For a given latitude ϕ and longitude λ, corresponding GRASP coordinates (x and y) are found using:

$$x_1 = \frac{\cos\phi \sin(\lambda - \lambda_0)}{\cos c} \tag{1}$$

$$y_1 = \frac{\cos\phi_0 \sin\phi - \sin\phi_0 \cos\phi \cos(\lambda - \lambda_0)}{\cos c} \tag{2}$$

from which GRASP coordinates are computed:

$$x = x_1(R_{Earth} \cdot a) + L_x/2$$

$$y = y_1(R_{Earth} \cdot a) + L_y/2$$

Here ϕ_0 is the central latitude, λ_0 the central longitude, L_x and L_y the domain sizes in native coordinates (units meters) in respectively x-, and y-direction, and a is a scaling factor chosen such that stretching as a result of the translation is minimized. The denominator ($\cos c$) is given by:

$$\cos c = \sin\phi_0 \sin\phi + \cos\phi_0 \cos\phi \cos(\lambda - \lambda_0)$$

Translation from GRASP x and y to latitude ϕ and longitude λ is done using the inverse equations:

$$\phi = \sin^{-1}\left(\cos c \sin\phi_0 + \frac{y_1 \sin c \cos\phi_0}{\rho}\right) \tag{3}$$

$$\lambda = \lambda_0 + \tan^{-1}\left(\frac{x_1 \sin c}{\rho \cos\phi_0 \cos c - y_1 \sin\phi_0 \sin c}\right) \tag{4}$$

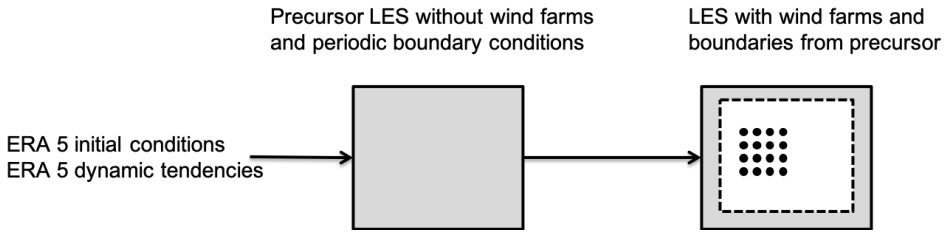

Figure 1. Schematic of the LES setup. ERA5 initial conditions and dynamic tendencies are prescribed to a precursor simulation with periodic boundary conditions. A second (cursor) LES is driven with boundary conditions from the pre-cursor simulation.

where

$$\rho = \sqrt{x_1^2 + y_1^2}$$

$$c = \tan^{-1} \rho$$

Input & boundary conditions

Mesoscale models are usually nested in large scale models by prescribing the values of the hosting model to the edges of the mesoscale model domain. In principle, such a method could be used for nested LES simulations as well, but it requires very large simulation domains to allow for sufficient development of turbulence in the LES. To overcome this, LES models are usually run with periodic boundary conditions and prescribe the large-scale boundary conditions only as tendencies, i.e. the state variables contain an extra forcing term to account for the large-scale processes. This setting to run an LES coupled to a large-scale NWP model has been extensively described in [Neggers et al., 2012] and [Schalkwijk et al., 2015]. We use ERA5 fields for the large-scale boundary conditions. At the bottom of the LES domain, we prescribe a Charnock parameter (α) from which a roughness length (z_0) is computed:

$$z_0 = \alpha \frac{u_*^2}{g}$$

where u_* is the friction velocity in m/s at the surface and $g = 9.81$ m/s^2 the local gravitational acceleration. We use a constant value for the Charnock parameter of $\alpha = 0.0185$ everywhere [Wu, 1980].

With the use of a concurrent pre-cursor simulation [Stevens et al., 2014] (an LES without wind farms that runs in parallel to the actual wind farm simulation), the turbulent free-stream wind conditions are prescribed at the edges of the simulation domain. Figure 1 schematically depicts the setup of the LES domain and the boundary conditions.

Turbine parameterisation

GRASP uses an actuator disk parametrisation as described by [Meyers and Meneveau, 2010]. This parametrisation only needs information about the power curve, thrust curve, rotor diameter and hub height. This information is publicly available or can be estimated with good accuracy. The parametrisation calculates the drag forces (using the thrust curve) and rotational forces (using the power curve) based on the local wind speed, taking the actual induction into account. Individual yaw control based on the local wind direction is applied to the turbines.

Output

Two types of files were produced from the simulations:

- Hourly averaged horizontal slices (sampling rate of once per 30 seconds) at each vertical level up to around 200m and every other level from 200 to at least 600m height.
- Single columns (profiles) for various coordinates at each vertical level up to at least 600m. Coordinates are chosen to coincide with previous and present measurement campaigns at the site and additional points near the corners of the domain.

The nudging zone (where cursor values are nudged to precursor values) was removed from the slices. The resulting files therefore contain 460^2 horizontal coordinates, rather than the native 512^2 as was mentioned above.

All profile output locations are shown in figure 2.

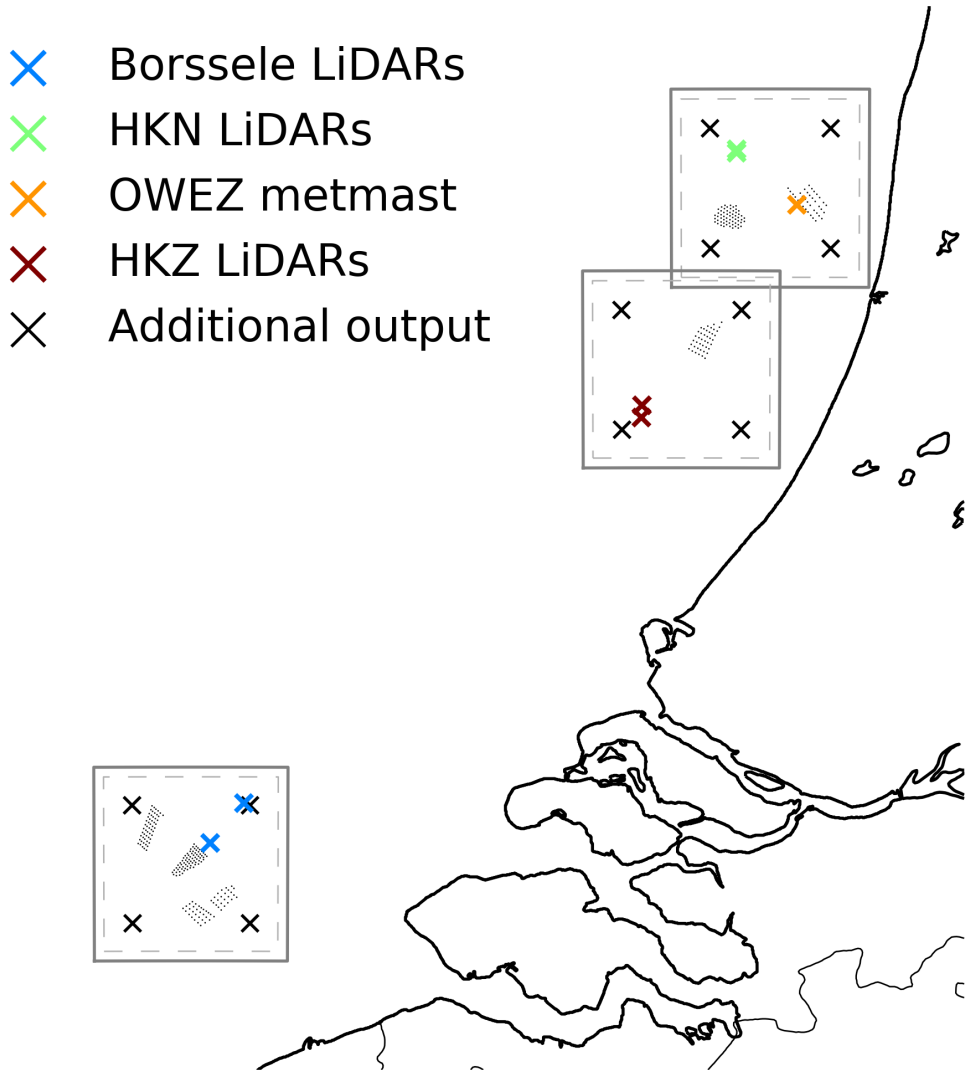

Figure 2. All profile output locations. Coloured markers indicate locations coinciding with measurement campaigns. The LES domains are shown in gray. The dashed line represent nudging zones.

Validation

In each of the wind farm zones for which the LES runs have been performed, LiDARs have been deployed for varying time periods during planning and/or operation of the wind farms present. The LES simulations that we performed included writing columns of various atmospheric quantities at the exact points of the LiDARS. Using both data sets, we have validated the LES data for the overlapping time periods.

We evaluate the model in comparison to observations by computing the correlation coefficient (ρ), bias, mean absolute error (MAE) and root mean square error (RMSE). We compute these as follows:

$$\rho = \frac{\sum(x_i - \bar{x})(y_i - \bar{y})}{\sqrt{\sum(x_i - \bar{x})^2}\sqrt{\sum(y_i - \bar{y})^2}} \tag{5}$$

$$\text{bias} = \bar{y} - \bar{x} \tag{6}$$

$$\text{MAE} = \frac{1}{N}\sum|y_i - x_i| \tag{7}$$

$$\text{RMSE} = \sqrt{\frac{1}{N}\sum(y_i - x_i)^2} \tag{8}$$

where overbars indicate sample mean values of that quantity:

$$\bar{q} = \frac{1}{N}\sum q_i$$

summation signs indicate sums over iterator i for all N values, where N is the sample size, x_i indicates an observed value and y_i indicates a modelled value.

Borssele

Two LiDARs have been deployed in the Borssele wind farm zone, see figure 3. LiDAR 1 was situated over 10 km away from any turbine, for the period of 11th June 2015 to 27th February 2017. LiDAR 2 was situated 2 km away from the closest turbine and operated from 12th February 2016 to 7th July 2016. Due to the proximity of LiDAR 2 to the present wind farms, we expect a distinguishable wake effect with respect to LiDAR 1 for certain wind conditions e.g. for south-westerly winds.

A comparison of wind speeds is done by scatter plot (figure 4) and by fitting a Weibull curve on the frequency distribution (figure 5). The scatter plots at both locations show good agreement between observations and simulation, both showing biases of 0.1 m/s or lower. A slight wind speed dependent bias may be recognized, as wind speeds measured $\gtrsim$25 m/s mostly lie above the 1:1 line. At the same time, low wind speeds in the observations also appear to be limited from below at a value slightly higher than zero, which is not the case in the model.

The wind speed distributions of figure 5 show that GRASP is well capable of capturing the wind climate with respect to observations. The shape parameters k lies within a 0.1 margin, whereas the scale parameter A lies within a 0.05 m/s margin. When comparing the scale factor A between LiDAR 2 and that of the overlapping LiDAR 1 data, one recognizes the wake effects of the Belgium wind farms. In the observations, the difference in A between LiDAR 1 and LiDAR 2 is 0.419, whereas in GRASP this difference is 0.246.

Wind direction agreement is illustrated in figure 6 by means of a scatter plot. Only points with a corresponding wind speed > 2 are included in the analysis as wind direction is not well defined for very low wind speeds. The circular correlation coefficient as indicated in the figure by ρ is computed as described by [Jammalamadaka, S. Rao and SenGupta, A., 2001]. We can recognize the prevalent wind direction by the higher number of points around the southwest quadrant. Some biases are observed which we suspect are due to instrument errors as we do not observe such biases at the other sites. Otherwise, a bias of nearly 20° is somewhat troublesome.

We further consider data at heights other than the 100m data which were presented above. Figure 7 illustrates the biases and correlations of wind speed (top panels) and direction (bottom panels) as a function of height up to 200m. The wind speed shows an increase in both correlation and bias with height. The increasing bias may be due to increasing wind speed magnitudes with height, inflating the bias signal. The increase in correlation may be due to smaller relative wind speed variability (e.g. turbulence intensity). The wind direction signal shows no clear height dependence.

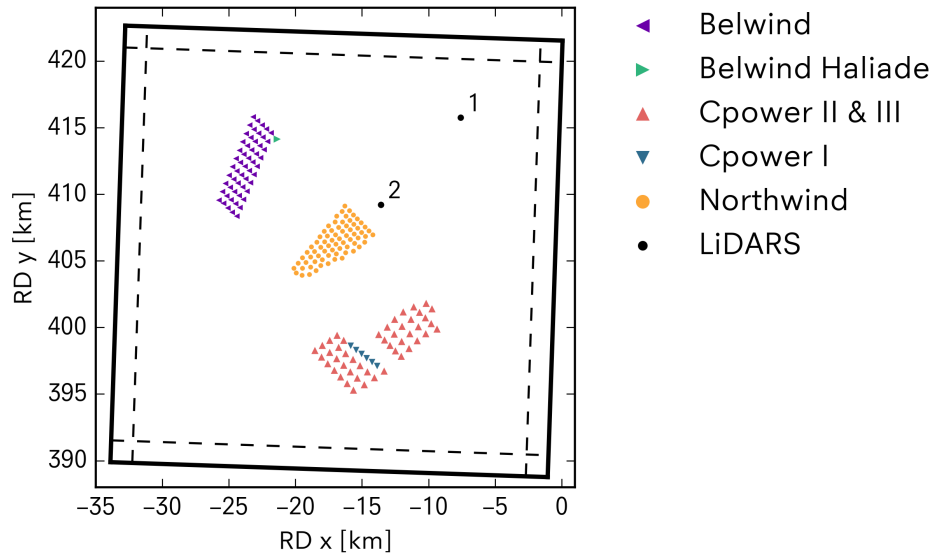

Figure 3. Schematic layout of the LES simulation. Distinction between markers is used to indicate different turbine models.

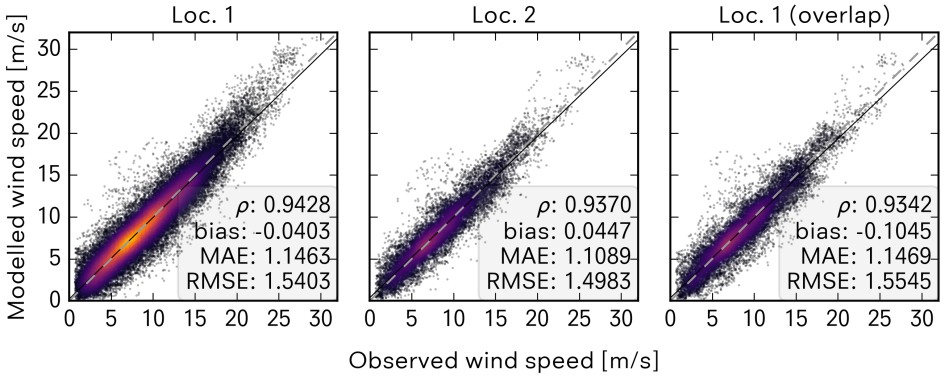

Figure 4. Simulated wind speeds compared to observed 100m wind speed at locations of LiDAR 1 (left), LiDAR 2 (centre) and LiDAR 1 including only data from the measurement period of LiDAR 2 (right). The LES is logarithmically interpolated to 100m from its adjacent model levels. The dashed gray line shows the 1:1 ratio, the thin black line shows the linear least squares fit (coefficients: $y_1 = 0.971x + 0.224$ [left panel], $y_2 = 0.961x + 0.374$ [centre], $y_{overlap} = 0.949x + 0.348$ [right]).

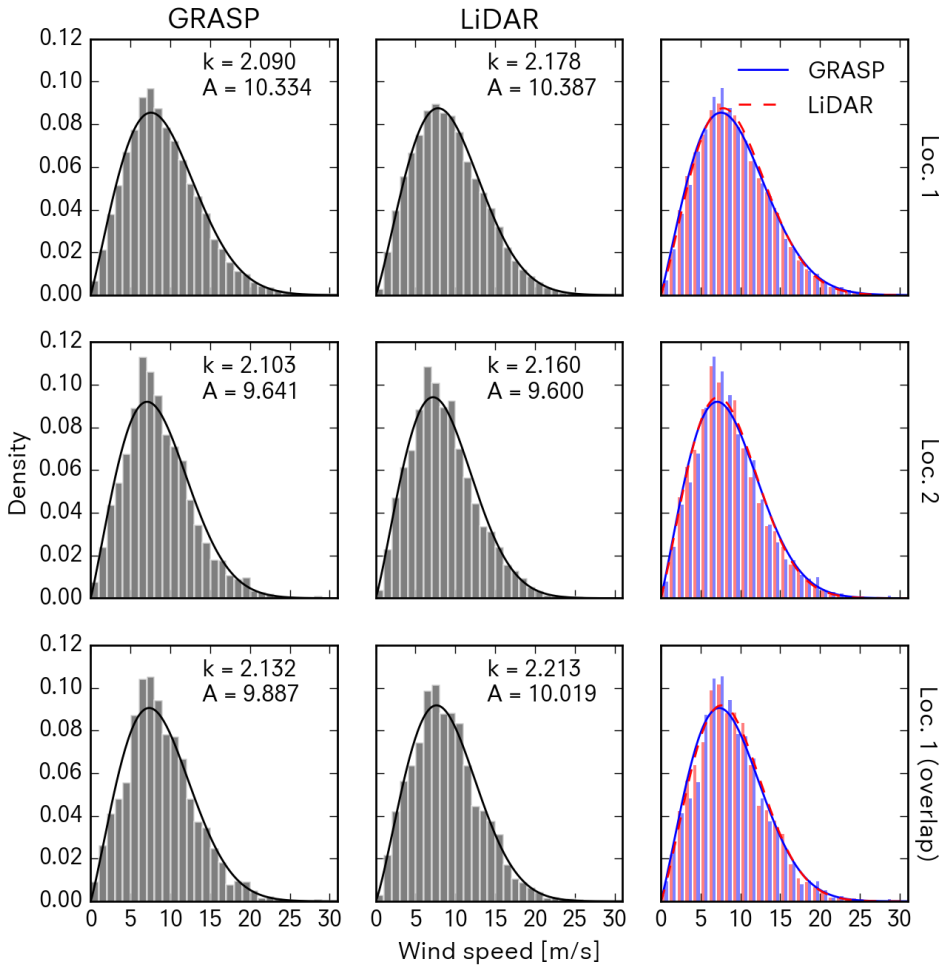

Figure 5. Wind speed histograms with Weibull distribution fits of GRASP and LiDAR for both locations. The full measurement period of the LiDARs at location 1 and 2 is shown in resp. the top and middle panels. The bottom panels show a subset of data from location 1 that coincides with the measurement period at location 2. The rightmost panels show the same histograms as the leftmost and centre panels in a single frame for easy side-by-side comparison.

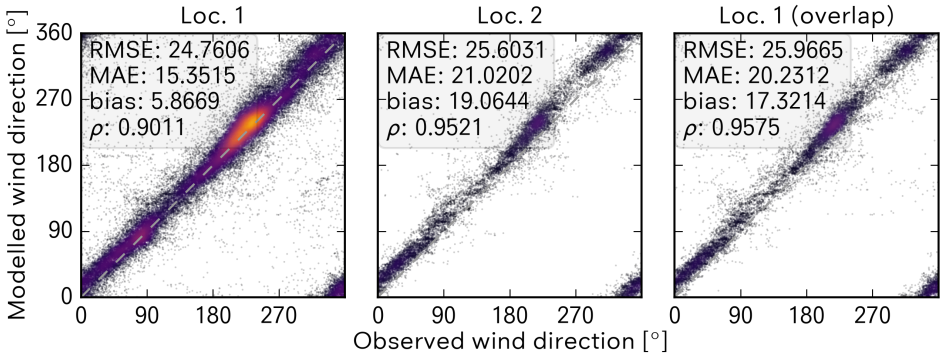

Figure 6. Wind direction of simulated wind compared to observed wind direction at 100m height, at locations of LiDAR 1 (left panel), LiDAR 2 (centre) and LiDAR 1 including only data from the measurement period of LiDAR 2 (right). The wind direction in GRASP is linearly interpolated to be comparable to the 100m observation. The dashed gray line indicates the 1:1 ratio.

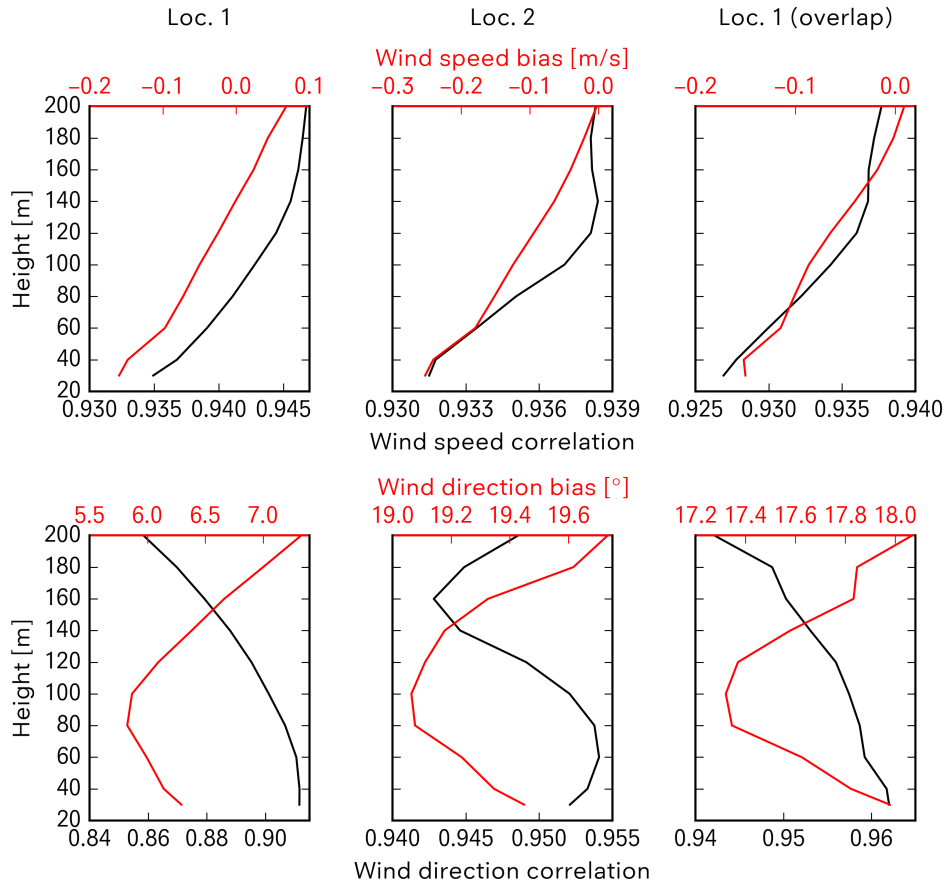

Figure 7. Correlation and bias of wind speed (top panels) and direction (bottom panels) at all heights for which there are observations. Biases are shown in red (top x-axis), correlations in black (bottom x-axis).

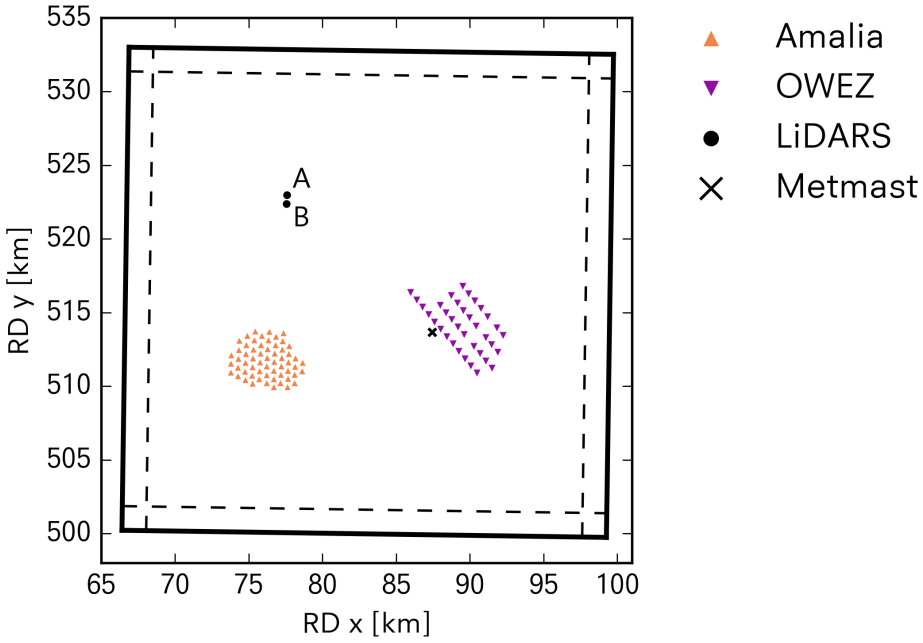

Figure 8. Schematic layout of the LES simulation on operational HKN wind farms.

HKN

Two measurement campaigns were performed in the HKN zone. A metmast was deployed before construction of the OWEZ wind farm and has measured until well after the wind farm became operational. A period of two years, coinciding with measurements, is simulated with GRASP. During this period, both the OWEZ and Amalia wind farms were operational. The second measurement campaign involved deploying 2 LiDARS adjacent to a future wind farm site. A period of one year has been simulated coinciding with the LiDAR campaign.

The two LiDARs are sufficiently close together (about 600m apart) that we do not expect a significant difference in outcome of longterm analyses. Any differences are largely due to natural variability in the system (e.g. due to the limited measurement period, measurement errors, model sampling rate, to name a few).

Comparison to LiDARs is only done for 2017 data. Comparison to the metmast is only done for 2009 and 2010 data. OWEZ has been operational during these 2 years.

From the skill parameters shown in figure 9 we find that GRASP performs well at compared to the LiDAR measurements. At the OWEZ metmast, thus very close to an operational wind farm, GRASP has a notable bias. The bias does not seem particularly pronounced at wind speeds where wakes are strongest (5 - 10 m/s) so we cannot readily conclude the bias is due to an inaccurate modelling of the wake effects. Further analysis is necessary to explain this bias. We note that [Duncan et al., 2019] also report an overestimation of the modeled wind speeds at the OWEZ met mast, even after filtering of the wind directions in which wake effects can be expected.

Figure 10 shows wind speed distributions of the same data as figure 9. Regarding comparison to the LiDARs, a slightly fatter tail is present in the model data. This is recognized in the scatter plots (figure 9) as points at high wind speeds mostly lying above the 1:1 line. Comparison to the metmast (figure 10, bottom right panel, dashed and solid lines) confirm our previous conclusion; a bias across all wind speeds. This is concluded from the red dashed line being slightly shifted with respect to the solid blue line. Its peak is also higher as a result of the normalization.

Figure 11 shows scatterplots of measured and modeled wind directions at the locations of the LiDARs and at the metmast. The error statistics at both LiDAR locations are very similar and markedly better than those at the Borssele zone (6). The wind direction errors at the metmast location are higher than those at the LiDAR locations. This is also apparent from the scatter plot itself (right panel). Parts of the data seem to be clustered around limited ranges of values, apparent as vertical streaks in the scatter plot. From detailed analysis at different measured heights we find varying degrees of this clustering (not shown in this report). We therefore do not attribute this to errors in the model, but rather to errors in the observations.

Correlation and bias at different heights are shown in figure 12. Regarding wind speed (top panels), we see a slight increase in correlation with height, but also increasing bias at lower levels for both LiDARs. For the met mast, the hieght dependent errors show no clear trend. Regarding wind direction (bottom panels) we see no particular signal for different heights.

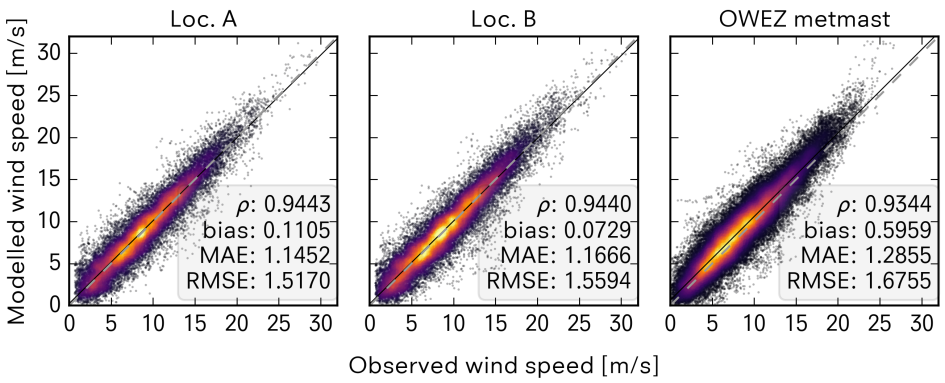

Figure 9. Scatter plot of modelled wind speed vs. observed wind speed. LiDARs A and B are compared at 100m, with GRASP logarithmically interpolated to this height. The metmast is compared at 116m. The dashed gray line shows the 1:1 ratio, the thin black line is a linear fit (coefficients: $y_A = 0.985x + 0.251$ [left], $y_B = 0.984x + 0.225$ [centre], $y_{OWEZ} = 0.994x + 0.649$ [right]).

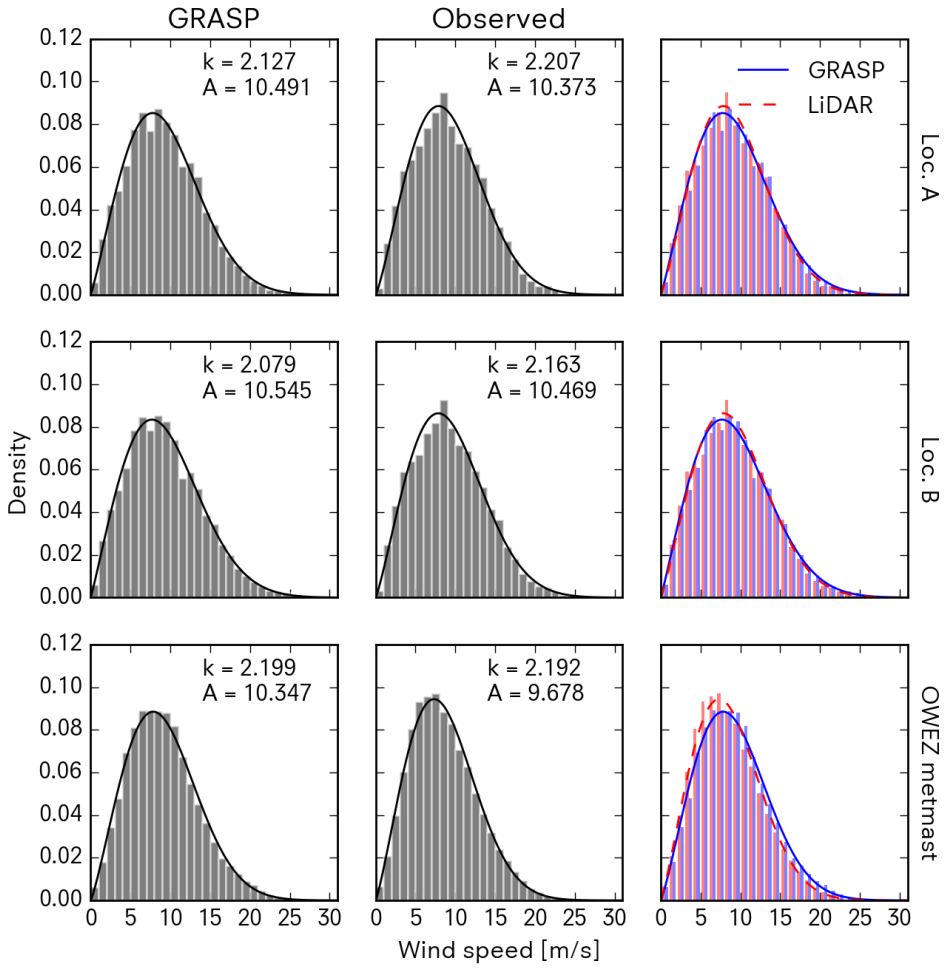

Figure 10. Wind speed histograms with Weibull distribution fits of GRASP and observations for each location. The rightmost panels show the same histograms as the leftmost and centre panels in a single frame for easy side-by-side comparison.

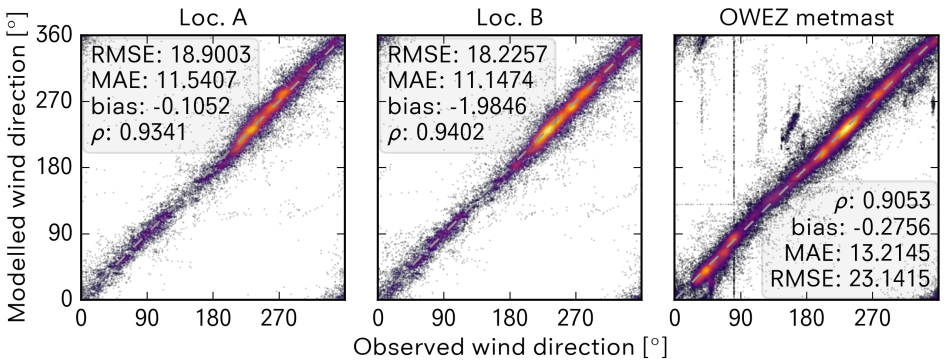

Figure 11. Scatter plot of the direction of modelled wind vs. observed wind at 100m for the LiDARs and 116m for the metmast. GRASP wind direction is derived from linearly interpolated vector components to this height. The dashed gray line shows the 1:1 ratio line.

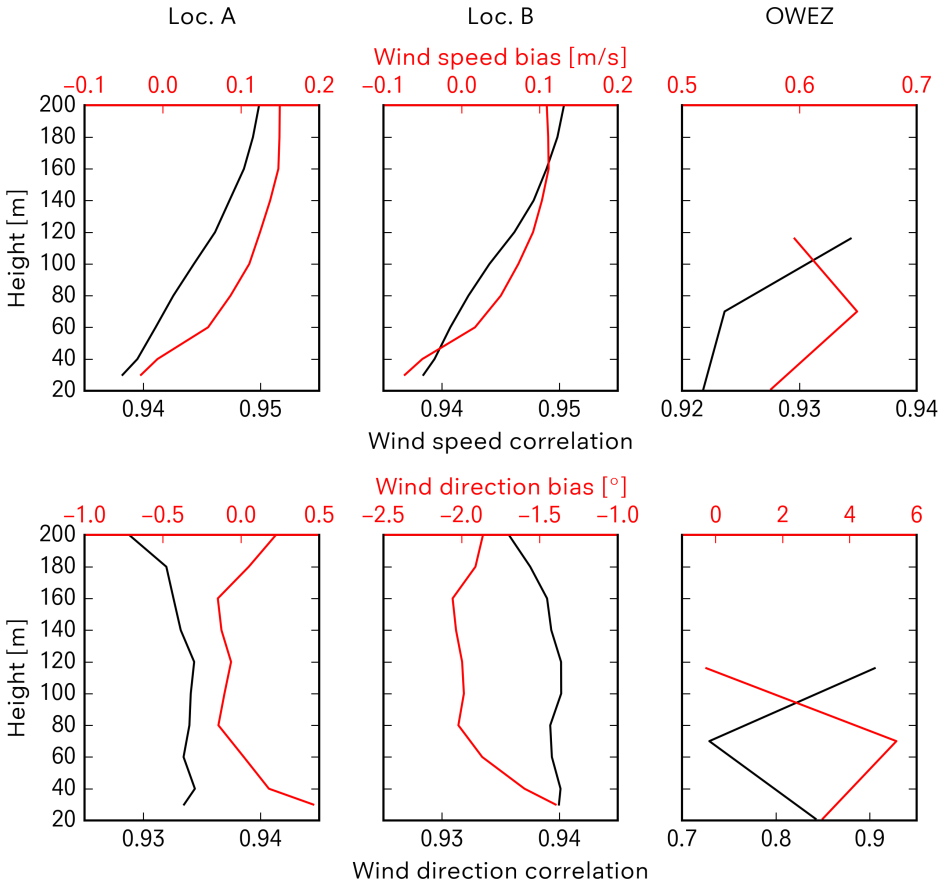

Figure 12. Correlation and bias of wind speed (top panels) and direction (bottom panels) at all heights for which there are observations. Biases are shown in red (top x-axis), correlations in black (bottom x-axis).

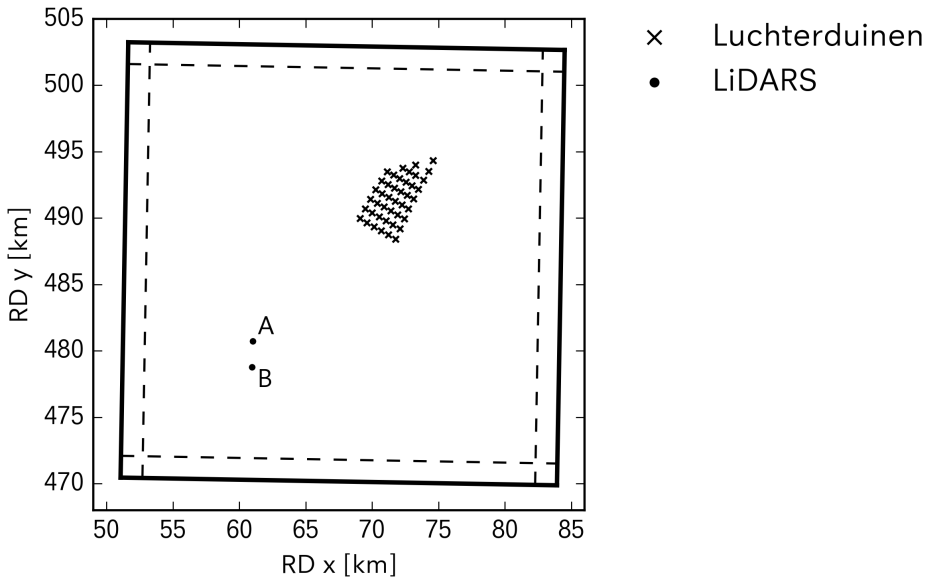

Figure 13. Schematic layout of the LES simulation centered on Luchterduinen and the HKZ LiDARs.

HKZ

Two LiDARs have been deployed in the HKZ zone, see figure 13. The LES simulation has been performed for the years 2016, 2017 and 2018 up to July 30th. We compare this to LiDAR data available from July 1st, 2016 to May 23rd, 2018. Both LiDARs are relatively close to each other (about 2km apart) and quite far from the nearest wind farm (Luchterduinen). Also, as southwesterly winds are generally most prevalent over the North Sea, we do not expect to see much effect of the nearby wind farms in the observations and expect similar outcome between LiDARs.

Figure 14 confirms the small difference in outcome as scores are very similar for both LiDARs. As is also apparent from figure 9, GRASP performs well for these locations, with biases below 0.1 m/s.

The wind speed distributions of figure 15 show a similar signal to the distributions from the HKN site (figure 10). Namely a slightly fatter tail in the GRASP data (which was also recognized as points above the 1:1 ratio line in the scatter plot) but generally good agreement between model and observations.

The modelled wind direction is also in good agreement with the observed directions, showing biases of less than a degree (figure 16).

Skill scores at heights other than the 100m presented above show an increase in wind speed correlation with height, as well as increasing bias (figure 17, top panels). The wind direction correlation seems to decrease with height, whereas the bias shows only a weak variance with height, staying just within a single degree bias.

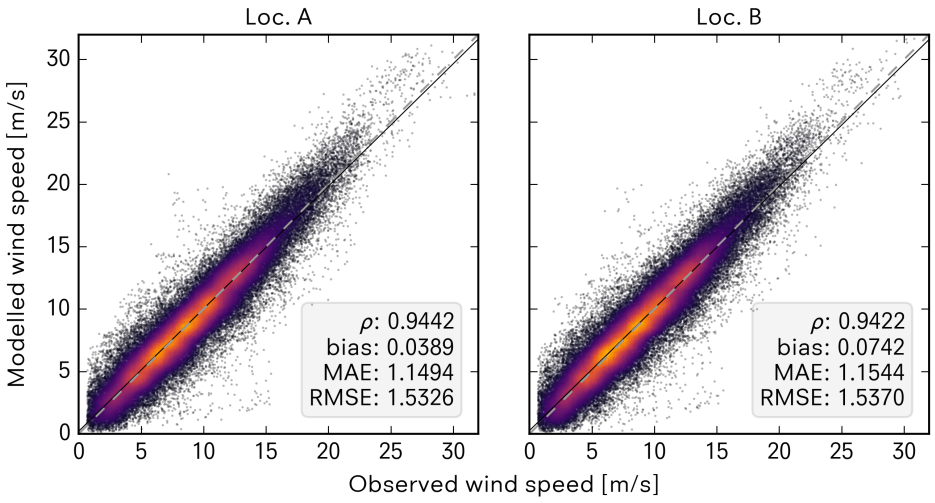

Figure 14. Scatter plot of modelled wind speed vs. observed wind speed. LiDARs A and B are compared at 100m, with GRASP logarithmically interpolated to this height. The dashed gray line shows the 1:1 ratio, the thin black line is a linear fit (coefficients: $y_A = 0.981x + 0.210$ [left], $y_B = 0.979x + 0.266$ [right]).

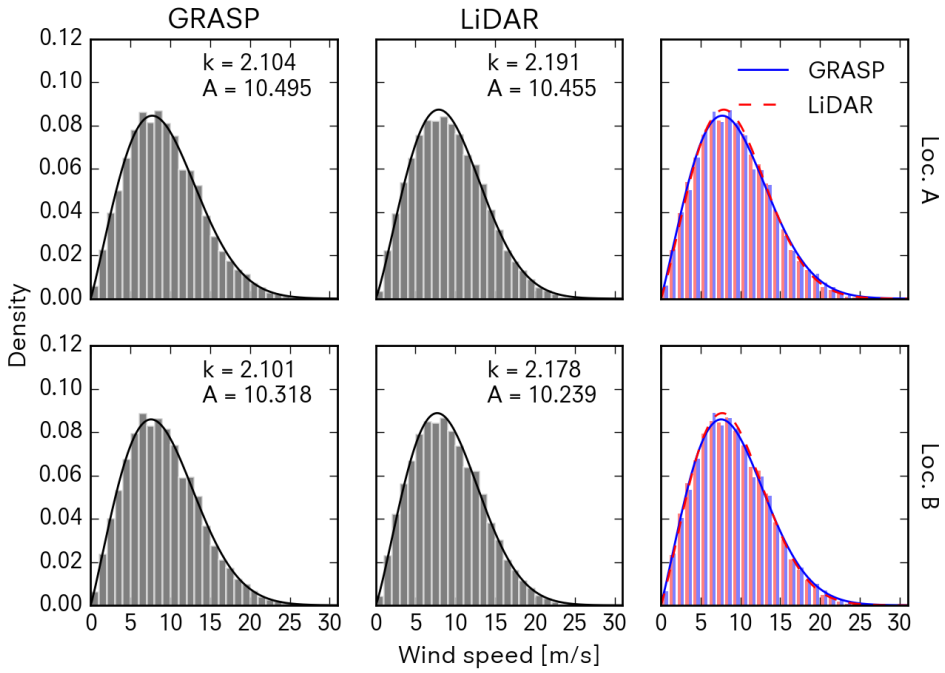

Figure 15. Wind speed histograms with Weibull distribution fits of GRASP and observations for both locations.

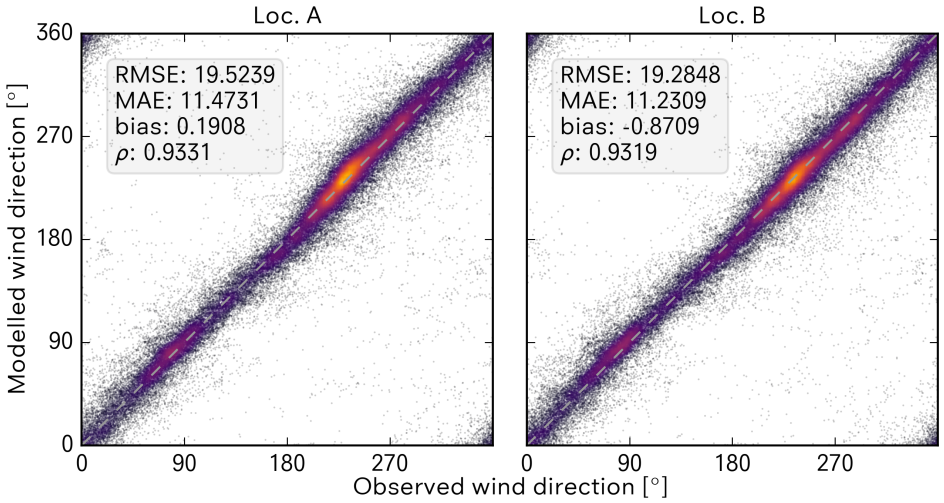

Figure 16. Scatter plot of the direction of modelled wind vs. observed wind at 100m. GRASP wind direction is derived from linearly interpolated vector components to this height. The dashed gray line shows the 1:1 ratio line.

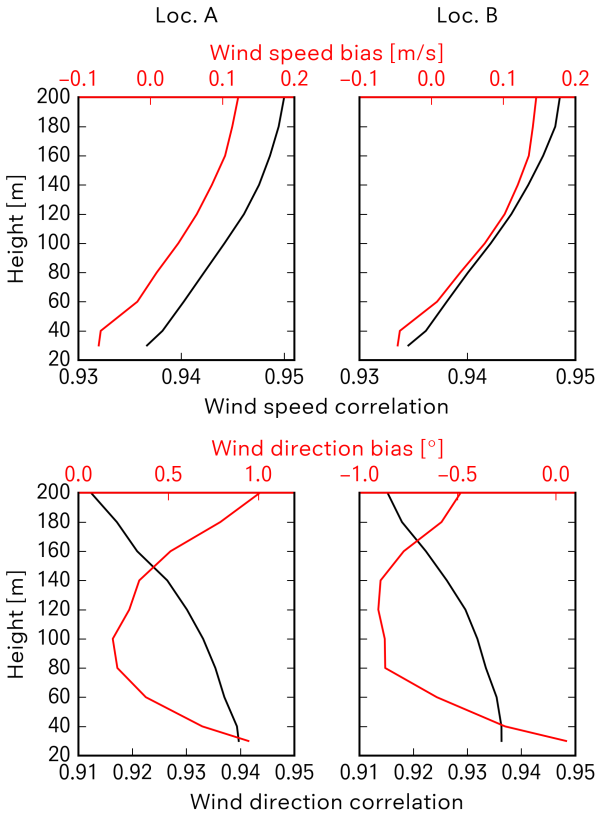

Figure 17. Correlation and bias of wind speed (top panels) and direction (bottom panels) at all heights for which there are observations. Biases are shown in red (top x-axis), correlations in black (bottom x-axis).

Conclusions

This document describes the set-up and validation results of LES runs at three sites where Dutch Offshore Wind Farms are being developed. The LES runs have been peformed with ERA5 boundary conditions and include wake effects of existing wind farms.

Validation results show that GRASP mean wind speeds compare well to the LiDAR measurements at all sites. In almost all cases the wind speed bias was less than or slightly higher than 0.1 m/s, which can be considered accurate compared to typical biases of other wind atlases. The only notable exception was the OWEZ met mast, where GRASP showed an overprediction of the wind speed of nearly 0.6 m/s. More analysis is needed to establish whether this overprediction is due to modelling errors or observational errors.

For the mean wind direction, the GRASP results at the Hollandse Kust Noord and Hollandse Kust Zuid sites are very close to the observed wind directions: not more than 2 degrees difference. For the Borssele zone, the wind direction bias is far higher: 6 degrees for location 1 and almost 20 degrees for location 2. However, this can most likely be attributed to measurement errors and further research is needed to verify this. Furthermore, a comparison with other mesoscale or reanalysis model data should be performed to draw more conclusions about the quality of the LES data compared to other modelling approaches.

References

Duncan et al., 2019. Duncan, J. B., Wijnant, I. L., and Knoop, S. (2019). DOWA validation against offshore mast and LiDAR measurements. Technical report.

Heus et al., 2010. Heus, T., Van Heerwaarden, C. C., Jonker, H. J., Pier Siebesma, A., Axelsen, S., Van Den Dries, K., Geoffroy, O., Moene, A. F., Pino, D., De Roode, S. R., and De Arellano, J. V. G. (2010). Formulation of the Dutch Atmospheric Large-Eddy Simulation (DALES) and overview of its applications. *Geoscientific Model Development*, 3(2):415–444.

Jammalamadaka, S. Rao and SenGupta, A., 2001. Jammalamadaka, S. Rao and SenGupta, A. (2001). *Topics in Circular Statistics*.

Meyers and Meneveau, 2010. Meyers, J. and Meneveau, C. (2010). Large Eddy Simulations of large wind-turbine arrays in the atmospheric boundary layer. In *48th AIAA Aerospace Sciences Meeting Including the New Horizons Forum and Aerospace Exposition*.

Neggers et al., 2012. Neggers, R. A., Siebesma, A. P., and Heus, T. (2012). Continuous single-column model evaluation at a permanent meteorological supersite. *Bulletin of the American Meteorological Society*.

Schalkwijk et al., 2012. Schalkwijk, J., Griffith, E. J., Post, F. H., and Jonker, H. J. J. (2012). High-performance simulations of turbulent clouds on a desktop PC. *Bulletin of the American Meteorological Society*.

Schalkwijk et al., 2015. Schalkwijk, J., Jonker, H. J., Siebesma, A. P., and Bosveld, F. C. (2015). A year-long large-eddy simulation of the weather over Cabauw: An overview. *Monthly Weather Review*.

Stevens et al., 2014. Stevens, R. J., Graham, J., and Meneveau, C. (2014). A concurrent precursor inflow method for Large Eddy Simulations and applications to finite length wind farms. *Renewable Energy*.

Wu, 1980. Wu, J. (1980). Wind-stress coefficients over sea surface near neutral conditions - a revisit.